

Particle size effects in Ru/CNF catalysts during supercritical water gasification of glycerol



Christopher Hunston ^{a,b}, David Baudouin ^{a,*}, Leo Koning ^a, Ayush Agarwal ^{a,c}, Oliver Kröcher ^{a,b}, Frédéric Vogel ^{a,d}

^a Bioenergy and Catalysis Laboratory, Paul Scherrer Institut (PSI), 5232 Villigen PSI, Switzerland

^b Institute of Chemical Sciences and Engineering (ISIC), École Polytechnique Fédérale de Lausanne (EPFL), 1015 Lausanne, Switzerland

^c School of Architecture, Civil and Environmental Engineering (ENAC IIE GR-LUD), École Polytechnique Fédérale de Lausanne (EPFL), 1015 Lausanne, Switzerland

^d Institute for Biomass and Resource Efficiency, Fachhochschule Nordwestschweiz (FHNW), 5210 Windisch, Switzerland

ARTICLE INFO

Keywords:

Supercritical water gasification
Ruthenium nanoparticles
Methanation
Particle size effect
Catalyst stability

ABSTRACT

Ru/CNF catalysts of different Ru nanoparticle (NP) sizes (0.9–2.7 nm) were assessed for their performance in continuous supercritical water gasification (SCWG) of glycerol. A structure sensitivity of Ru was demonstrated, with high initial turnover frequencies (TOF) for Ru NPs smaller than 1.2 nm. Deactivation happens essentially through: 1) coking, which occurs more readily at low Ru surface densities and is limited to nanometric layers, and 2) sintering, which led to final NP sizes ranging from 2 to 3 nm independent of the catalyst loading (1–30 wt % Ru). A correlation between TOF and the density of surface Ru atoms was found, with an optimal surface density ($0.4\text{--}0.7 \text{ atom}_{\text{Ru,sfc}} \text{ nm}^{-2}$) resulting in high initial and high steady-state TOFs, allowing longer lifetimes through the delay of coke formation. CNF as a support enables high metal loadings with optimal performance, which could help in decreasing the volume of high-pressure vessels and hence the cost of SCWG plants, making this technology even more attractive.

1. Introduction

Supercritical water gasification (SCWG) has drawn considerable attention in recent years as a clean and renewable synthetic natural gas (bio-SNG) production technology. As water acts as the solvent and reactant in these conditions, no drying step is required to convert biomass feeds of high moisture content, leading to higher gas production efficiencies ($\approx 70\%$) compared to conventional conversion technologies [1]. Combustible gases (CH_4 and H_2) can easily be produced from the catalytic conversion of wet biomass at moderate SCWG temperatures (375–450 °C) at which CH_4 formation is favoured. For this however, an active gasification and methanation catalyst is required [2–7]. A lot of work has been performed on SCWG catalysts in order to guarantee high activity and long lifetimes, [6,8,9] as well as to understand the main deactivation mechanisms, namely leaching, [10–13] sintering, [14,15] poisoning [16–18,15] and coking [15,19,20].

Many studies already showed the superiority of ruthenium-based catalysts for SCWG, be it in terms of gasification/methanation activity or in terms of stability towards leaching and sintering [8,10,16,21,22].

However, Ru is known to exhibit structure sensitivity in several catalytic reactions such as Fischer-Tropsch synthesis, [23,24] ammonia synthesis [25,26] and ammonia decomposition [27,28]. This is also the case for the methanation reaction, where size sensitivity was observed for Ru/TiO₂, [29,30] Ru/C [31] and single crystals [32]. The reason for this size sensitivity is thought to arise from B_5 sites, introduced by van Hardeveld and van Montfoort, [33] which are a combination of five under-coordinated “step-edge” atoms creating a three-dimensional adsorption site for reactive species (*i.e.* CO or N₂). For the methanation reaction, CO dissociation seems to be the rate-limiting step and occurs preferentially at under-coordinated sites, as shown over a Ni surface [34]. On Ru, *ab initio* studies at 400 °C reported lower free energy barriers during CO methanation at stepped Ru surfaces through multiple hydrogen transfer steps leading to an easier C–O bond cleavage and the subsequent formation of H₂C and water [35]. The computational study of Shetty *et al.* [36] showed a lower CO dissociation energy barrier at “hollow” Ru sites (allowing high coordination of CO) than on stepped surfaces, indicating that specific sites (such as B_5 sites) are highly active for CO activation. These very active sites have high probabilities of

* Corresponding author.

E-mail address: david.baudouin@psi.ch (D. Baudouin).

being found at defined Ru nanoparticle (NP) diameters, as they are purely geometrical features. Based on the work of van Hardeveld and van Montfoort, [33] Jacobsen et al. [25] showed that there was a high concentration of B_5 sites on Ru NPs of 1–3 nm in diameter. They suggested that the increase in ammonia synthesis activity was due to the disappearance of the smallest NPs (< 1 nm) due to sintering, which led to larger crystals containing more B_5 sites. Indeed, Ru NPs smaller than 0.8 nm exhibit very few B_5 sites, as there are not enough atoms available to form these special ensembles. Czekaj et al. [37] performed DFT calculations of Ru clusters of different sizes supported on graphitic carbon layers. They showed that Ru clusters only stabilised in given geometries on graphite, and that 1.5 nm Ru NPs contained more B_5 sites (i.e. 12) than 1.0 nm Ru NPs (i.e. 6), which is in line with the high activity observed with Ru/C catalysts composed of small Ru NPs (1.2–1.4 nm) [17].

Most fundamental studies on Ru-based SCWG catalysts were performed with activated carbon (AC) as support, as it possesses a high specific surface area and exhibits good mechanical stability in supercritical water (SCW). Unfortunately, using AC as catalyst support is far from optimal for several reasons. On the one hand, the high surface area of AC mainly arises from micropores, which are often too small (< 1 nm) to welcome Ru NPs, and are prone to rapid surface area losses and pore blockage by coke deposits, eventually leading to mass transfer limitation and catalyst deactivation [15,38,39]. On the other hand, the heterogeneity, density and intrinsic activity of AC make it difficult to precisely evaluate the different deactivation mechanisms, e.g. coking or sintering.

De Vlieger et al. showed that carbon nanofibers (CNF) could be used in continuous SCWG, highlighting the good stability of unsupported and supported CNF [19]. They followed up with another study using Ru/CNF for aqueous-phase reforming of acetic acid, proving the good gasification activity and deactivation resistance of this material in SCW [40]. CNF were also shown to be an ideal support for particle size effect studies due to their high pore volume, mostly open porosity (micropore free), high specific surface area, as well as their purity and inertness [41]. Furthermore, the CNF structure makes it an ideal support for the analysis of supported metal NPs, particularly in transmission electron microscopy (TEM) [42].

The geometry of a particle is known to greatly depend on the atmosphere it is exposed to, even at low partial pressures [43]. Hence, the effect of particle size on Ru activity in SCWG may therefore greatly differ from the theory. Despite a few preliminary studies, [44,45] to the best of our knowledge, the effect of the Ru NP size on the gasification activity has never been thoroughly studied in SCWG conditions. In this paper, we elucidated the particle size effect in a model SCWG system, using Ru/CNF catalysts of different Ru NP sizes to gasify aqueous glycerol solutions to CH₄.

2. Experimental

2.1. Materials and methods

Commercial carbon nanofibers (CNF, NC7000, Nanocyl) were used as catalyst support. They were first sieved to 0.50–0.80 mm, then purified in 1 M KOH (2 h, reflux), washed in deionised water (DI H₂O) until the filtrate was neutral, dried overnight (110 °C in air), and sieved again to the fraction of interest (0.50–0.80 mm). The purified support was then impregnated with RuNO(NO₃)₃ (31.3% Ru, Alfa Aesar) or RuCl₃ · xH₂O (38% Ru, Alfa Aesar) dissolved in DI H₂O with the incipient wetness method (IWI). The solution concentration was adapted to reach the desired catalyst loading (x_{Ru}) based on the support pore volume ($V_p = 3.6 \text{ cm}^3 \text{ g}^{-1}$), determined by addition of water to mimic the synthesis method. The impregnated CNF were dried at 110 °C (air, 15 h) before being reduced in a quartz reactor (i.d. = 45 mm, L = 600 mm, with a fritted disc in the middle) for 4 h at 300 °C (5 °C min⁻¹) in H₂/N₂ (5:95 vol/vol, 150 mL min⁻¹). After, the reactor was cooled down to room temperature and the catalysts were passivated by letting air diffuse

through the quartz reactor. This procedure allowed the formation of a RuO₂ oxide layer at the surface of Ru(0) particles in a controlled and reproducible way, which will be readily reduced back under reactive conditions [17]. The Ru/CNF catalysts were eventually sieved again to 0.50–0.80 mm before being loaded in the catalytic reactor. At this stage, the catalysts were referred to as “fresh”. High-purity glycerol ($\leq 99.7\%$, Carl Roth GmbH & Co. KG) was diluted in DI H₂O to reach glycerol concentrations ranging from 6 wt% to 20 wt% and was used as biomass model feed for the SCWG experiments.

2.2. Continuous SCWG setup

The catalytic performance was investigated on a SCWG setup used in a previous study [10] (Konti-I, P&ID shown in Fig. S1). A high-pressure pump (Knauer 80 P) fed the aqueous glycerol (6–20 wt%) into the system at 28.5 MPa. A series of three heaters was used to bring the feed up to 405–410 °C at the beginning of the catalyst bed. A 316 L stainless steel tube (SITEC-Sieber Engineering AG) was used as fixed-bed plug-flow reactor (L = 460 mm, i.d. = 8 mm, o.d. = 14.3 mm), the flow configuration was top to bottom. The Ru/CNF catalyst bed was situated in the middle of the reactor (260 mm from reactor entry), held in place by three sizes of stainless steel wire mesh – 0.08, 0.25 and 0.50 mm placed on top of a hollow stainless steel rod. The rest of the catalyst bed was filled with α -Al₂O₃ beads (0.8 mm diameter, 0.03 cm³ g⁻¹ porosity, Alfa Aesar), which was used as inert filling material. A heat exchanger was located at the exit of the catalytic reactor to cool down the effluent. A back pressure regulator (BPR, Tescom), protected by a 15 µm frit, maintained the system at the desired pressure (28.5 MPa). After the BPR, the effluent entered a phase separator from where the liquid and gas phases exited the setup. The latter was cooled through a Peltier element (1–4 °C) to remove the water before being analysed online with a µGC (Inficon). An automated sampler located between the BPR and the phase separator was used to collect the liquid effluent at defined times on stream (TOS). Samples (2 min sampling time, 10–15 mL) were taken every 30 min to monitor the carbon and ruthenium concentrations. A target WHSV_{gRu} of 4000 g_{org} g_{Ru}⁻¹ h⁻¹ was selected to ensure a final carbon conversion below 50% and thus monitor the catalyst activity (i.e. turnover frequency, TOF) in the kinetic regime.

The absence of internal mass transfer limitation was verified through the Weisz-Prater criterion [46], which was in an acceptable range (0.03 \ll 0.3) for all catalytic tests performed in this study.

2.3. Analytics

The gas produced from the catalytic experiments was analysed online with a µGC 3000 series (Inficon) having two different columns (Molsieve, 10 m x 320 µm x 30 µm and PLOTQ, 8 m x 320 µm x 10 µm) with TCD detectors. The former analysed H₂, O₂, N₂, CO, and CH₄ in He as carrier gas at 120 °C, 25 psi. The latter analysed CO₂ and C_{2,3} in Ar as carrier gas at 70 °C, 20 psi. The carbon content of the unfiltered liquid effluent was analysed on a Dimatoc2000 (DIMATEC) total (TC), total inorganic (TIC) and total organic (TOC) carbon analyser. The instrument determined the TC by oxidising the carbon into CO₂ at 850 °C in a quartz reactor containing a Pt/SiO₂ catalyst. The TIC was determined by converting the carbonates to CO₂ at 160 °C with addition of H₃PO₄ (42.5%) in a quartz reactor filled with porous silica gel beads. The TOC was eventually determined by subtraction (TOC = TC – TIC).

The carbon gasification efficiency GE_C was determined by Equation 1.

$$GE_C (\%) = \frac{\dot{n}_{C,gas}}{\dot{n}_{C,feed}} \cdot 100 \% \quad (1)$$

by knowing the flow of carbon in the produced gas ($\dot{n}_{C,gas}$) and the amount of carbon entering the system ($\dot{n}_{C,feed}$) per unit of time.

The carbon conversion (X_C) was calculated with Equation 2.

$$X_C (\%) = \frac{TOC_{feed} - TOC_{out}}{TOC_{feed}} \cdot 100 \% \quad (2)$$

where TOC_{feed} and TOC_{out} are the amounts of organic carbon present in the feed and the process waters, respectively.

The specific surface area (SSA) and the pore volume (V_p) were measured by N_2 physisorption (77 K) on an Autosorb-1 (Quantachrome). The samples were outgassed in dynamic vacuum (10^{-6} bar) for a minimum of 3 h at 300 °C. The SSA was calculated according to the Brunauer-Emmett-Teller (BET) model, the total pore volume was determined at a relative pressure $p/p_0 = 0.99$.

After synthesis, the catalyst loading was verified by calcination in static air (900 °C, 10 °C min⁻¹, 12 h) in a muffle oven (Nabertherm). The ash content of the support was then subtracted and the residual ash content was corrected, as the ruthenium was completely oxidised (RuO_2). The loading determination through calcination was in good agreement with the calculated loading from the impregnation step (error ≤ 10%), validating this characterisation method.

The Ru dispersion (D_{TEM}) was determined from TEM micrographs acquired with a JEOL JEM 2010 microscope operated at 200 keV and equipped with a LaB₆ cathode. Images were recorded by a slow scan CCD camera (4008 × 2672 pixels, Orius Gatan Inc.). High-resolution TEM images were acquired on a probe-corrected JEOL JEM-ARM200F (NeoARM) microscope equipped with a cold-field emission gun operated at 200 keV and a Gatan OneView camera. The instrument could be operated in TEM or STEM modes. Samples were prepared on lacey carbon grids (Ted Pella Inc.) using ethanol to disperse the ground catalyst. For each catalyst sample, a thorough qualitative analysis was performed and representative micrographs were carefully selected to determine a particle size distribution (PSD). The minimum sample size for each analysed catalyst was 160 particles, except for the fresh 30% Ru/CNF and both spent 1%Ru/CNF catalysts (sample size ≈ 100). The histogram bin size for the PSD was selected by following the guidelines of Alxneit [47] to ensure a statistically representative particle size determination. The Ru NP diameters were corrected for the formation of the oxide passivation layer in contact with air, which was reported to reach 0.6 nm [48]. For Ru NPs smaller than 1.2 nm, the size was corrected by the ratio of the Ru(0) and RuO₂ bulk densities, as performed in other studies [49,50]. The dispersion was then calculated according to Equation 3,

$$D_{TEM} (\%) = \frac{\sum_i Ru_{sfc,i}}{\sum_i Ru_{tot,i}} \cdot 100 \% \quad (3)$$

where $Ru_{sfc,i}$ and $Ru_{tot,i}$ are the amount of surface and total Ru atoms in the i^{th} NP, calculated from the geometrical equations published by van Hardeveld and Hartog [51], linking the particle diameter to the number of atoms for a truncated bipyramid (see Fig. S2 and Table S1). The detailed calculation steps can be found in the supporting information (SI). The reported Ru NP diameters refer to the main mode obtained from the PSDs (Figs. S3-S6).

The turnover frequency (TOF) was used to compare the activity of the different catalysts and was calculated with Equation 4,

$$TOF \left(\frac{mol_c}{mol_{Ru,sfc} \cdot min} \right) = \frac{\dot{n}_{C,feed} \cdot X_C}{n_{Ru} \cdot D_{TEM}} \quad (4)$$

where $\dot{n}_{C,feed}$ is the mole flow rate of carbon into the system, n_{Ru} is the moles of Ru in the catalyst bed and D_{TEM} is the Ru dispersion. Thus, $n_{Ru,sfc} = n_{Ru} \cdot D_{TEM}$. The initial activity (TOF_{30min}) was calculated with the fresh catalyst dispersion, while the steady-state activity (TOF_∞) was calculated with the dispersion of the spent catalyst.

The reaction rate (r) was used to evaluate the impact of dispersion loss on the activity of the catalyst and was calculated with Equation 5.

$$r \left(\frac{mol_c}{mol_{Ru,tot} \cdot min} \right) = \frac{\dot{n}_{C,feed} \cdot X_C}{n_{Ru}} \quad (5)$$

Thermogravimetric analyses (TGA, Mettler Toledo TGA/SDTA 851e) were performed on the CNF support as well as on selected catalyst samples (fresh and spent). Approximately 10 mg of sample were loaded in an Al_2O_3 crucible. The samples were first heated up to 110 °C in air (5 °C min⁻¹, 30 min hold) to get rid of the moisture. The temperature was then increased to 900 °C (5 °C min⁻¹). Analyses were performed with air as reactive gas (10 mL min⁻¹) and Ar (10 mL min⁻¹) as protective gas.

The Ru concentration in process waters was analysed using an Agilent 7700x ICP-MS with the following parameters: RF power 1350 W, sampling depth 10 mm, carrier gas (Ar) flow rate 0.93 L min⁻¹. Each sample was acidified to 1% HNO_3 using TraceSELECT™ nitric acid before analysis. Two isotopes (⁹⁹Ru and ¹⁰¹Ru) were monitored at an integration time of 0.20 s in transient analysis mode. External calibration with commercial standards from Inorganic Ventures (ICP Precious Metals Std) was done using five standard points with concentrations of 0, 0.01, 0.1, 1, and 10 $\mu\text{g L}^{-1}$.

3. Results and discussion

3.1. Catalyst characterisation

The main support and catalyst properties are summarised in Table 1. When comparing the as-received support (CNF AR) and the purified one (CNF), one can see that treatment in KOH did not alter the support properties, as the SSA and pore volume remained similar. The catalyst synthesis did not affect the SSA too much either, with values ranging from $297 \pm 14 \text{ m}^2 \text{ g}^{-1}$ (1%Ru/CNF 2) to $226 \text{ m}^2 \text{ g}^{-1}$ (30%Ru/CNF). However, the pore volume decreased linearly with increasing Ru loading. The decrease in SSA with increasing metal loading was explained by the increase in material density (Fig. S7, right). However, the decrease in pore volume was not fully explained by the density (Fig. S7, left). The volume occupied by the Ru NPs is the most likely explanation for the pore volume decrease, as the 30%Ru/CNF catalyst exhibited the most pronounced loss in V_p .

By preparing the catalysts by incipient wetness impregnation, the following hypothesis can be made: 1) 100% of the support pore volume was filled by the Ru precursor solution, 2) the solution was distributed homogeneously throughout the pore volume. Hence, the presence of Ru salts inside the CNF are expected to remain there upon thermal treatment, as observed with other metallic salts in SBA-15 [52,53]. Statistically, 12 ± 7% of Ru should be located on the inside of the fibres used in this work. This is in line with results from Winter *et al.*, who proved that Co and Pd NPs were located inside carbon nanotubes (up to 15% and 34%, respectively) after synthesis [54].

The catalyst synthesis method applied in this work yielded very small Ru NPs, with D_{TEM} reaching 67–71% for the 1%Ru/CNF and 5%Ru/CNF catalysts ($d_p = 0.9$ –1.1 nm, Fig. 1). Another 5%Ru/CNF catalyst not shown in this work, synthesised with the same technique, yielded Ru NPs of the same size ($d_p = 1.0$ nm, $D_{TEM} = 69\%$). These figures also

Table 1
Support and catalyst characteristics after impregnation.

Material ^a	SSA ($\text{m}^2 \text{ g}^{-1}$)	V_p ($\text{cm}^3 \text{ g}^{-1}$)	x_{Ru} (%)	D_{TEM} (%)
CNF_AR ^b	288	3.9	–	–
CNF	311 (19)	3.3 (0.3)	–	–
1%Ru/CNF_1	286	2.3	1.4 (0.3)	67
1%Ru/CNF_2	297 (14)	2.4 (0.1)	1.1 (0.3)	71
5%Ru/CNF_1	263 (16)	2.0 (0.1)	4.6 (0.3)	67
5%Ru/CNF_Cl ^c	297	2.2	5.1 (0.3)	69
10%Ru/CNF	283	1.8	10.4 (0.3)	59
15%Ru/CNF	287 (11)	1.8 (0.1)	16.0 (0.3)	47
20%Ru/CNF	268	1.6	20.6 (0.8)	51
30%Ru/CNF	226	1.1	32.3 (0.5)	35

^a Catalysts synthesised from $RuNO(NO_3)_3$ unless stated otherwise. ^b As-received material. ^c Synthesised from $RuCl_3 \cdot xH_2O$. Standard deviations ($n = 3$) of selected catalysts are given in parentheses.

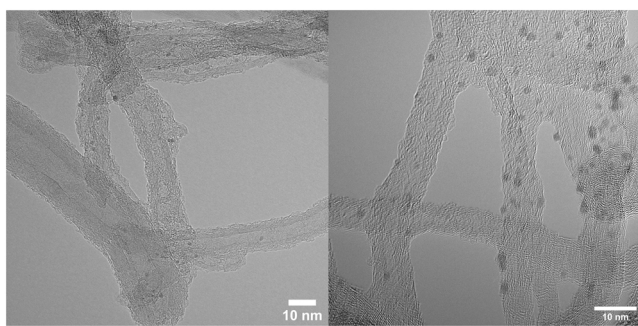


Fig. 1. High-resolution TEM micrographs of the fresh 1%Ru/CNF_2 (left, magnification: 250k) and 5%Ru/CNF_1 (right, magnification: 600k) catalysts. The small Ru NPs appear as darker spots.

highlight the high reproducibility of the synthesis method. The use of a chloride salt instead of nitrosyl nitrate led to a slightly higher dispersion.

Very small Ru NPs (≤ 1.1 nm, $D_{\text{TEM}} \geq 67\%$) were achieved with catalyst loadings up to 5%, while higher Ru contents led to a decrease in D_{TEM} , from 59% for 10%Ru/CNF down to 35% for 30%Ru/CNF. However, even the high loading of the latter catalyst yielded a main Ru NP diameter mode at 2.0 nm, which remains relatively small. The evolution of d_p and D_{TEM} as function of Ru loading is shown in Fig. 2 for the fresh catalysts. These results show that small Ru NPs, i.e. high metal dispersion, can easily be achieved on CNF with a facile synthesis method, even at high loadings.

3.2. SCWG of glycerol over Ru/CNF catalysts

In Fig. 3, an example of a catalytic SCWG experiment is shown with the 10%Ru/CNF catalyst (see Figs. S8-S14 for all other experiments). The carbon gasification efficiency (GE_C) and conversion (X_C) overlapped, indicating that all the converted carbon ended up in the gas phase (the discrepancy observed for the first GE_C data point is explained by the significant variation in gas flow at the start of an experiment). 10%Ru/CNF exhibited a high initial activity, before stabilising towards 30–35% conversion. Because steady state was not reached for all catalysts, an extrapolation was performed in order to have a more accurate estimation of the steady-state values for X_C and TOF and ensure a better comparison between the different catalysts. Both parameters were hence fitted with an exponential decay function (optimised through a Levenberg-Marquardt iteration algorithm). An example is shown for the 10%Ru/CNF catalyst in Fig. S15.

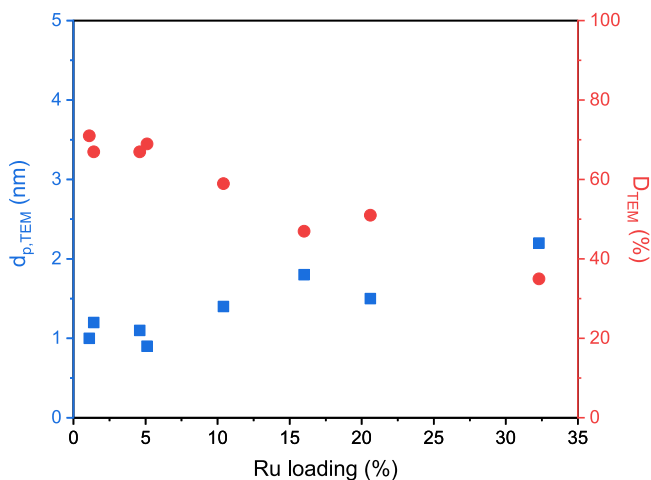


Fig. 2. Ru NP diameter mode ($d_{p,\text{TEM}}$, blue squares) and catalyst dispersion (D_{TEM} , red circles) as a function of Ru loading for all synthesised catalysts.

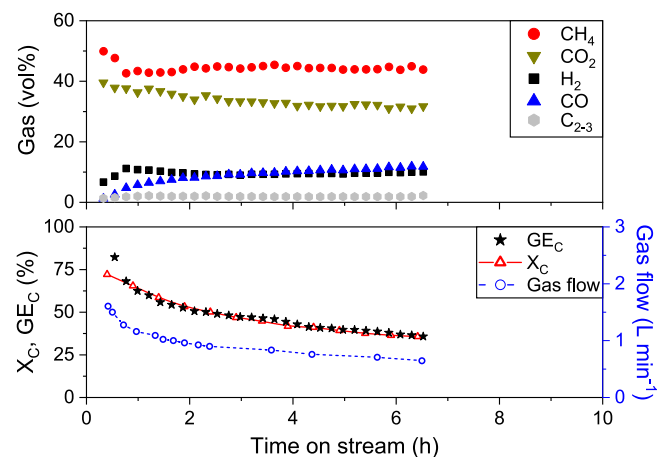


Fig. 3. SCWG of glycerol (20 wt%) over 10%Ru/CNF. The gas composition is shown in the top graph, the carbon gasification efficiency (GE_C , stars) and conversion (X_C , triangles) are shown in the bottom graph together with the produced gas flow (blue circles). Conditions: $p = 28.5$ MPa, $T = 405$ °C, $\text{WHSV}_{\text{Ru}} = 4047 \text{ g}_{\text{org}} \text{ g}_{\text{Ru}}^{-1} \text{ h}^{-1}$.

The carbon conversion was reported for all experiments (see Fig. S16), where two distinct trends were observed. The catalysts exhibiting a lower activity (15%Ru/CNF, 20%Ru/CNF, 30%Ru/CNF) had initial conversions in the range 50–65%, stabilising towards $\approx 20\%$ at steady state. On the contrary, catalysts of lower loadings and smaller Ru NP diameters (1%Ru/CNF_2, 5%Ru/CNF_Cl, 5%Ru/CNF_1, 10%Ru/CNF) showed initial conversions higher than 65%, stabilising at steady-state values around 40–50%. Both 1%Ru/CNF catalysts exhibited high initial conversions, but suffered from drastic deactivation. At the evaluated conditions, full conversion was initially achieved for the 5%Ru/CNF_Cl and 1%Ru/CNF_1 catalysts, preventing accurate estimations of an initial TOF.

To understand the implications of the different deactivation mechanisms, the effects of leaching, sintering and coking were assessed for this set of experiments.

We showed in a previous work that Ru leaching was negligible from activated carbon supports, with concentrations in the range $0.01\text{--}0.2 \mu\text{g L}^{-1}$, being close to thermodynamic models [10]. Ru NPs may exhibit a decreased metal-support interaction on CNF, as this support is known to be more inert than activated carbon due to its well-defined structure [55,56]. To investigate the effect of Ru loss, time-resolved ICP-MS was used to quantify the Ru loss from the Ru/CNF catalysts. The acquired data (Figs. S17 & S18) shows that the final Ru concentrations in the process waters were in the same range as for Ru/AC. Most catalysts exhibited a similar Ru loss trend i.e. higher amounts at the start before stabilising towards $0.06\text{--}0.12 \mu\text{g L}^{-1}$. The measured concentrations showed that the higher inertness of the support (compared to activated carbon) did not alter the metal-support interaction. Hence, leaching is thought to have a negligible effect on catalyst deactivation.

In the case of the 1%Ru/CNF_1 catalyst, it is interesting to note that the Ru concentration in the process waters suddenly increased (8-fold) after 3 h TOS, which coincided with the rapid decrease in X_C (Fig. S19). The reason for this Ru loss behaviour remains unclear. Changes in solvent properties around the Ru NPs could be the reason for this increase, as the density and the chemical composition of the medium rapidly changed due to the rapid loss in X_C . With a rapid change in X_C from 100% to 10%, the gaseous products were replaced mainly by glycerol and its degradation products. However, more experimental data is required to further conclude on the effect of rapid activity loss on the Ru loss increase.

As Ru leaching was shown to be negligible, the effect of sintering and coking were investigated together due to the impossibility of disentangling both effects in SCWG conditions. To do so, the SCWG activity

(TOF) of the different Ru/CNF catalysts was compared in Fig. 4, where the top graph regroups the experiments performed at $\text{WHSV}_{\text{gRu}} \approx 4000 \text{ g}_{\text{org}} \text{ g}_{\text{Ru}}^{-1} \text{ h}^{-1}$ and the bottom graph shows the 1%Ru/CNF catalysts tested at different WHSV_{gRu} (3000 and 9000 $\text{g}_{\text{org}} \text{ g}_{\text{Ru}}^{-1} \text{ h}^{-1}$). In the top graph of Fig. 4, all catalysts showed a similar trend in TOF throughout the experiments. The highest activity was recorded for 5% Ru/CNF_Cl, which also exhibited a very high dispersion (69%). Note however that this catalyst reached high initial conversions, close to the thermodynamic value, explaining the plateau observed initially. The other 5%Ru/CNF_1 catalyst was less active at the beginning of the experiment, but eventually stabilised at a steady-state TOF (TOF_{∞}) in the same range as the former catalyst ($\text{TOF}_{\infty} = 55$ and 47 min^{-1} , respectively). The activity of 10%Ru/CNF was slightly lower than both 5%Ru/CNF catalysts, but still significantly higher than the higher-loading catalysts. For the 15%, 20% and 30%Ru/CNF catalysts, the loss in activity was more pronounced and their TOF_{∞} were consequently lower ($26-28 \text{ min}^{-1}$). Looking at the 1%Ru/CNF catalysts (Fig. 4, bottom), the initial activity was much higher for 1%Ru/CNF_2 than for the other catalysts and reached $\text{TOF} = 152 \text{ min}^{-1}$ at $X_C = 64\%$, while 5% Ru/CNF_Cl was limited at 105 min^{-1} because of the high conversion ($X_C \approx 100\%$). Due to the relatively high initial conversion, the initial TOF of the 1%Ru/CNF_2 experiment might be underestimated. However, the TOF loss was very rapid in both 1%Ru/CNF experiments, leading to low final TOF values overlapping after $\text{TOS} = 4 \text{ h}$ and stabilising at 11 min^{-1} . The complete data set discussed here can be found in Table S2.

In Fig. 5, the initial TOF taken at 30 min TOS ($\text{TOF}_{30 \text{ min}}$), is presented as a function of catalyst dispersion. Note that the initial conversions of the 5%Ru/CNF_1 and 10%Ru/CNF catalysts being above 60% (70% and 76%, respectively), the $\text{TOF}_{30 \text{ min}}$ may be slightly underestimated (marked with an asterisk in Fig. 5). For catalyst dispersions

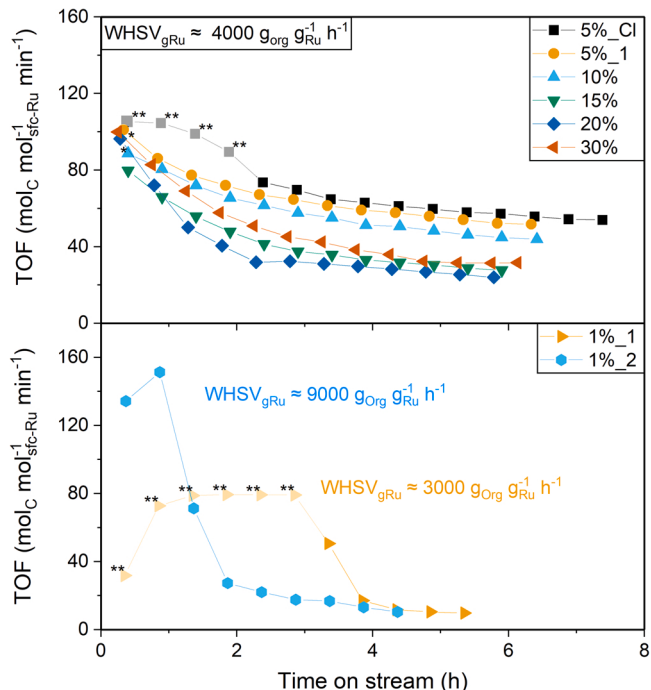


Fig. 4. TOF overview after SCWG of glycerol (6–20 wt%) over different Ru/CNF catalysts. The top graph shows Ru/CNF (5–30%) catalysts treated at $\text{WHSV}_{\text{gRu}} \approx 4000 \text{ g}_{\text{org}} \text{ g}_{\text{Ru}}^{-1} \text{ h}^{-1}$. The bottom graph shows the 1%Ru/CNF_1 and 1%Ru/CNF_2 catalysts treated at WHSV_{gRu} of 3000 and 9000 $\text{g}_{\text{org}} \text{ g}_{\text{Ru}}^{-1} \text{ h}^{-1}$, respectively. The shown TOFs were calculated with the fresh catalyst dispersion. Conditions: $p = 28.5 \text{ MPa}$, $T = 400-408 \text{ }^{\circ}\text{C}$. Data marked with two asterisks are left aside because $X_C \approx 100\%$. The points marked with one asterisk are slightly above the limit of $X_C = 60\%$.

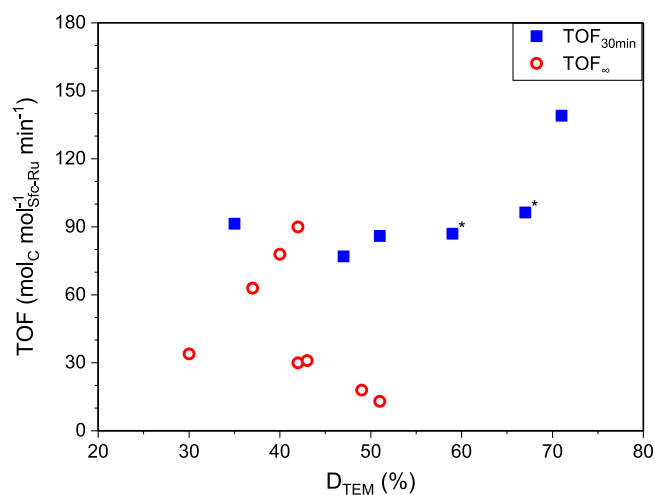


Fig. 5. Evolution of $\text{TOF}_{30 \text{ min}}$ (initial TOF taken at $\text{TOS} = 30 \text{ min}$) and TOF_{∞} as a function of catalyst dispersion. The asterisks indicate catalysts 5%Ru/CNF_1 and 10%Ru/CNF, whose high X_C (70% and 76%, respectively) may result in an underestimation of $\text{TOF}_{30 \text{ min}}$.

between 35% and 60%, the $\text{TOF}_{30 \text{ min}}$ remained relatively stable in the range $80-100 \text{ min}^{-1}$. However, very small Ru NPs ($D_{\text{TEM}} > 65\%$) presented a higher initial TOF than larger ones. This clearly evidences a particle size effect in SCWG over Ru-based catalysts and highlights the benefit of working with small Ru NPs around 1.0 nm. After the experiments, the spent catalysts were analysed by TEM and N_2 physisorption and the results are reported in Table 2. All catalysts suffered from dispersion loss, but to different extents as it can be observed in Fig. 6. Globally, the catalysts exhibiting the most significant dispersion losses were those with the highest initial values. The Ru NP size of all spent catalysts stabilised towards 2–3 nm, independent of the initial dispersion and loading. These results could suggest a thermodynamically-stable Ru NP size, as reported by Parker and Campbell [57] for gold NPs supported on TiO_2 . The pore volume generally increased by 5–10%, whereas the surface area decreased by 10–20%. Overall however, all catalysts exhibited excellent stability, which demonstrates the compatibility of the Ru/CNF catalytic system with supercritical water conditions.

The TOF_{∞} of all catalysts are presented in Fig. 5. As described previously, the dispersion of all tested catalyst decreased to values ranging from 30% to 50% after the gasification experiments. In contrast with the initial TOF values, TOF_{∞} were in disarray with values varying by a 2-to-3-fold factor for catalysts with final dispersions around 40–45%. Interestingly, the three high-loading catalysts (15%, 20%, 30%) showed similar TOF_{∞} around 32 min^{-1} , both 5% and the 10%Ru/CNF catalysts around $60-80 \text{ min}^{-1}$, while both 1%Ru/CNF catalysts exhibited very low TOF_{∞} values ($\approx 15 \text{ min}^{-1}$). These results suggest that the catalyst dispersion alone is not the only parameter influencing the steady-state catalyst activity.

In Fig. 6, the rate loss was reported as a function of the loss in D_{TEM} . The dashed line representing "rate loss = D_{TEM} loss" is an indication of the level at which the rate loss would be entirely caused by the loss of Ru dispersion. Since all catalysts lie above that line, another phenomenon than Ru NP sintering contributed to the observed deactivation. The impact of Ru loss by leaching or loss of catalyst debris being negligible, the other cause of catalyst deactivation in this study can only be coking. However, the impact of coking on mass transfer limitation to the inside of the CNF cannot explain the observed difference between the catalysts, assuming a constant fraction of Ru NPs anchored on the inside of the fibers (see Section 3.1). The share of deactivation caused by coking does not appear to be the same for all catalysts. Indeed, the two catalysts with the highest TOF_∞ in Fig. 4 exhibited the smallest difference between the rate loss and the reference line, indicating that coke had a lower impact

Table 2

Catalyst characteristics before and after catalytic testing.

Catalyst	fresh				spent			
	SSA (m ² g ⁻¹)	V _p (cm ³ g ⁻¹)	D _{TEM} (%)	d _{p,TEM} (nm)	SSA (m ² g ⁻¹)	V _p (cm ³ g ⁻¹)	D _{TEM} (%)	d _{p,TEM} (nm)
1%Ru/CNF_1	286	2.3	67	1.1	285 (12)	2.8 (0.1)	51	1.6
1%Ru/CNF_2	297 (14)	2.4 (0.1)	71	1.0	273	2.7	49	1.9
5%Ru/CNF_1	263 (16)	2.0 (0.1)	67	1.1	274	2.3	40	2.2
5%Ru/CNF_Cl	297	2.2	69	0.9	271	2.4	42	2.1
10%Ru/CNF	283	1.8	59	1.4	252	1.9	37	2.3
15%Ru/CNF	287 (11)	1.8 (0.1)	47	1.8	265	2.0	42	2.0
20%Ru/CNF	268	1.6	51	1.5	250	1.8	43	2.2
30%Ru/CNF	226	1.1	35	2.0	224	1.4	30	2.7

^a The main mode is reported from the PSD (see Figs. S3-S6). Standard deviations (n = 3) of selected catalysts are given in parentheses.

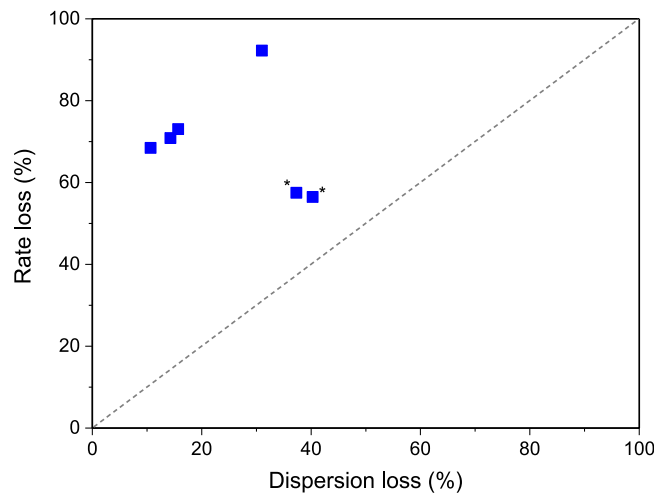


Fig. 6. Rate loss as a function of D_{TEM} loss for all Ru/CNF catalysts tested. The rate loss was calculated from the initial ($r_{30\text{min}}$) and the final (r_∞) rates. The asterisks indicate a possible rate loss underestimation (see Fig. 5).

on deactivation.

One could have expected the catalysts of higher loadings to sinter more significantly, because of the lower inter-particle distance. Indeed, Yin *et al.* [58] showed that a critical particle distance existed, up to which significant NP sintering occurred. In their study, Pt sintering could be avoided up to 900 °C through higher spacing between the NPs, either by using lower metal loadings or high surface area supports. However, the lowest D_{TEM} losses occurred for the higher-loading catalysts (15%, 20% and 30%Ru/CNF). The limited sintering data presented in this work suggests that, for all catalysts, the inter-particle distance must have been below this critical particle distance due to the high surface area of CNF.

Peng *et al.* [59] reported that a 5%Ru/AC catalysts exhibited an increased stability compared to its 2% analogue during isopropanol conversion (450 °C, 30 MPa), even though the dispersion of the former was lower. He showed that the coke formation rate was lower on the catalyst containing a higher fraction of Ru, although the Ru NPs were larger (5 nm vs. 3 nm). This is in line with the results presented here, showing that the dispersion was not the only factor affecting the stability of the catalyst. One reason for the 3-times higher activity and good stability of both 5%Ru/CNF catalysts with regard to other catalysts of same dispersion could be due to the density of active sites. Indeed, the metal loading can significantly vary between catalysts of similar dispersions.

To verify this hypothesis, TOF_{30min} and TOF_∞ were plotted as function of the surface density of active Ru (Ru_{sfc}) in the fresh and spent materials (Fig. 7). As described previously, the TOF_{30min} of 1%Ru/CNF_2 clearly stood out due to its very high initial activity at high space

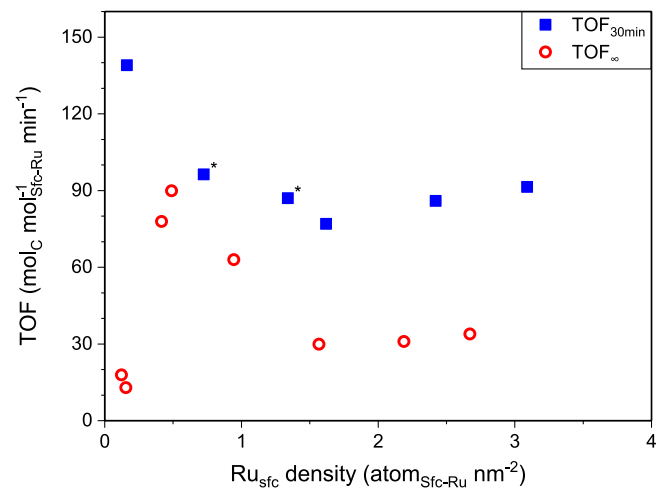


Fig. 7. Initial (TOF_{30min}, blue squares) and steady-state (TOF_∞, red circles) TOF after SCWG of glycerol over Ru/CNF catalysts as a function of the surface density of active Ru (Ru_{sfc}). TOF_{30min} was taken at TOS = 30 min. The asterisks indicate catalysts 5%Ru/CNF_1 and 10%Ru/CNF, whose high X_C (70% and 76%, respectively) may result in an underestimation of TOF_{30min}.

velocity. For the other catalysts, TOF_{30min} decreased before stabilising at higher Ru_{sfc} surface density (≈ 1.5 atoms_{Ru,sfc} nm⁻²). The smallest Ru NPs (0.9–1.2 nm) were clearly responsible for the high initial activity with Ru surface densities lower than 0.8 atoms_{Ru,sfc} nm⁻². However, the trend changed when looking at the steady-state data (TOF_∞), with an optimum Ru surface density appearing in the range 0.4–0.7 atoms_{Ru,sfc} nm⁻², corresponding to a catalyst of Ru NP diameter around 2.1 nm with a 4–8 wt%Ru loading and 260 m²g⁻¹ surface area. At higher Ru surface density, the steady-state trend matched the initial activity one, remaining constant with increasing Ru_{sfc} surface density. This is a strong indication that the steady-state catalyst activity can be increased by having the optimal amount of active sites at the catalyst surface. It is important to keep in mind that the mentioned Ru_{sfc} surface densities are average densities, and do not necessarily represent the reality when looking at the local surface density, especially for the low-loading catalysts (1%Ru/CNF). A catalyst synthesis method yielding high catalyst homogeneity and narrow particle size distribution as used here (Fig. 1) is likely of great importance.

As mentioned previously, coking may be one of the deactivation mechanisms leading to the rapid loss in activity for the 1%Ru/CNF catalysts. The extent of coking investigated by HR-TEM revealed that very little coke deposited on all spent catalysts. Except for the slight increase in Ru NP size, hardly any difference could be observed between the fresh and spent catalysts. However, in the case of the 1%Ru/CNF_2 catalyst treated at high space velocity, very thin carbon deposits could be observed at the surface of Ru NPs, as it can be seen from

representative images in Fig. 8. Note that these images were acquired at very low beam intensity and exposure to limit carbon deposition from the environment. The fact that this observation could only be made on the catalyst that suffered from the most severe deactivation supports coking as the source of deactivation together with sintering. This also suggests that deactivation by coking only occurred by the deposition of a thin layer of C at the surface of the metal.

To further investigate coke deposition, TGA was performed on the neat support, the 1%Ru/CNF and 5%Ru/CNF_{Cl} catalysts (Figs. 9 and 10). For the neat CNF support, a sharp weight loss was observed with a maximum at 590 °C. When Ru was loaded onto the CNF (1 and 5 wt%), the weight loss occurred at lower temperatures and over a longer range, with maximum rates at 570 and 550°C, respectively. The weight loss patterns were different for the fresh and both spent (1%Ru/CNF_1 and 1%Ru/CNF_2) catalysts. The former underwent constant weight loss, with one clear contribution in the DTG curve close to 600 °C. The spent catalysts exhibited broader differential profiles, with the weight-loss offset higher in temperature for 1%Ru/CNF_2 (≈ 510 °C vs. ≈ 460 °C). This indicated an altered/decreased activity of ruthenium for oxidising the support (especially for 1%Ru/CNF_2), which could be ascribed to Ru NP size increase and/or coke deposits. The catalyst treated at lower WHSV_{gRu} exhibited a similar initial oxidation activity to the fresh 1% Ru/CNF catalyst, although it required higher temperatures to fully oxidise the support and the carbon deposits. For 1%Ru/CNF_2 treated at higher WHSV_{gRu}, the initial weight-loss phase was similar to the neat CNF, showing that the Ru NPs had a low activity towards support oxidation. Only at temperatures above 600 °C could the support and coke be completely oxidised. This is in phase with HR-TEM results and supports that Ru was largely covered and blocked by coke.

TGA performed on the best-performing catalyst (5%Ru/CNF_{Cl}, Fig. 10) showed a completely different weight-loss trend. Indeed, the offset was shifted to a lower temperature for the spent catalyst (≈ 300 °C) compared to the fresh one (≈ 380 °C), while the differential profile looked similar. The maximum weight-loss rate of the spent catalyst was shifted to a slightly lower temperature (520 vs. 550 °C). The significant shift in temperature observed for the 5%Ru/CNF_{Cl} catalyst cannot be explained by deposited coke precursors of lower thermal stability than CNF because of the very small difference in the differential weight-loss curve. The reason for this shift in temperature remains unclear. For both loadings (1% and 5%), the spent catalysts lost slightly more weight than the fresh ones, indicating either a slight decrease in ash content due to the SCW conditions and/or an increase in the carbon fraction i.e. by coke deposition. The observed difference being small, it did not allow us to exclude one of the possibilities and we were not able to conclude on the impact of metal loading on coke deposition.

As discussed previously, a higher Ru NP density at the CNF surface seemed beneficial to maintain a high gasification activity (5%Ru/CNF vs. 1%Ru/CNF) and avoid catalyst deactivation by carbon deposits

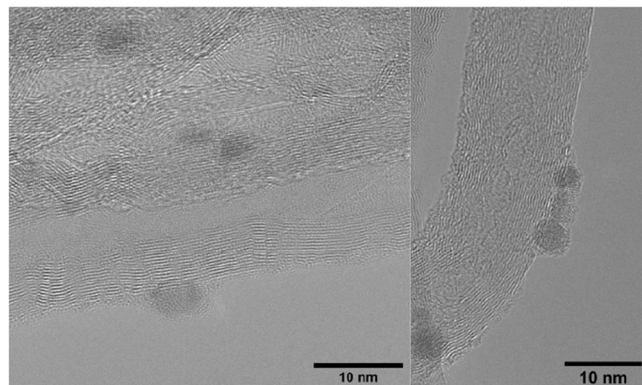


Fig. 8. HR-TEM images of the 1%Ru/CNF_2 catalyst treated at WHSV_{gRu} = 9000 g_{org} g_{Ru}⁻¹ h⁻¹. Magnification: 600kX left, 800kX right.

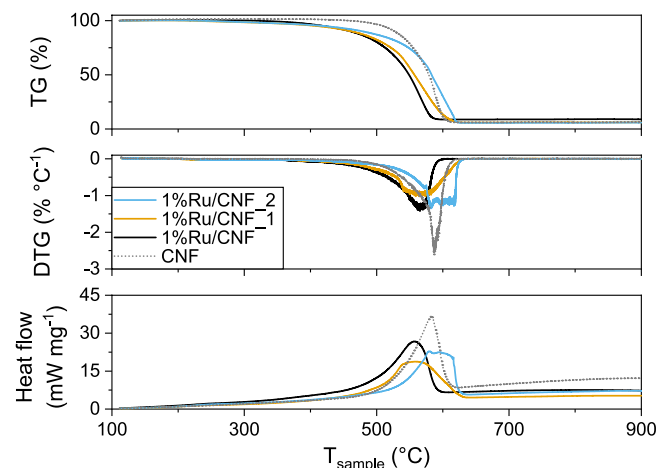


Fig. 9. Relative weight (TG, top), differential weight loss (DTG, middle), and heat flow (bottom) analyses for the fresh and spent 1%Ru/CNF catalysts.

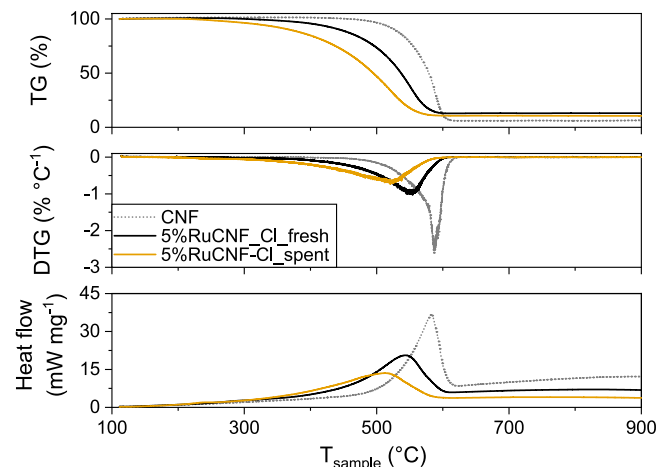


Fig. 10. Relative weight (TG, top), differential weight loss (DTG, middle) and heat flow (bottom) analyses of the neat support (CNF), the fresh and spent 5%Ru/CNF_{Cl} catalysts.

rapidly obstructing the access to the active sites, most probably by covering Ru NPs with nanometric layers of carbon.

4. Conclusions

We showed that Ru/CNF catalysts can successfully be used in continuous SCWG systems and exhibit high gasification activity and stability. Structure sensitivity of Ru was shown for the first time in SCWG conditions, with Ru NP diameters smaller than 1.2 nm leading to the highest initial activity. However, a combination of high initial dispersion and optimal surface ruthenium density was shown to be crucial to maintain a high steady-state activity. The optimal surface Ru density was found to be around 0.4–0.7 atom_{Ru,sfc} nm⁻², which is thought to help in delaying/suppressing coke formation by limiting carbon deposition on large Ru-free carbon surfaces. The loss of active phase from Ru/CNF catalysts being negligible, the observed catalyst deactivation was linked to a combination of coking and Ru NP sintering, systematically stabilising to 2–3 nm. Coking was found to occur in very small amounts and to be limited to nanometric layers on top of Ru NPs. With an optimal particle size and surface density identified, efforts must now go into improving the stability of Ru nanoparticles towards coking, for instance through doping of the carbon support or ruthenium to limit adsorption of unsaturated compounds.

Evaluating deactivation mechanisms in SCWG conditions is not straightforward, nevertheless Ru/CNF proved to be an ideal system to perform in-depth catalytic studies in SCWG conditions. This is mainly due to the well-defined CNF structure and high contrasts generated in TEM, as well as the large CNF pore volume (micropore-free) and surface area allowing high Ru loadings. The good stability of Ru/CNF catalysts gives new opportunities in the field of catalytic SCWG as it allows the preparation of highly dispersed and homogeneously distributed Ru nanoparticles. Its large open (non-microporous) surface allows a much higher loading than activated carbon at optimal Ru surface density, with optimised catalyst stability towards coking. Consequently, the volume of the catalyst fixed bed can be reduced, which should in turn reduce investment costs for SCWG processes, the latter being closely linked with the volume of a vessel at high pressures. The feasibility of using this catalyst on larger scales should however be assessed.

CRediT authorship contribution statement

Christopher Hunston: Investigation, Methodology, Validation, Formal analysis, Writing – original draft. **David Baudouin:** Conceptualization, Methodology, Validation, Writing – review & editing, Supervision. **Leo Koning:** Investigation, Formal analysis. **Ayush Agarwal:** Investigation, Validation, Formal analysis. **Oliver Kröcher:** Resources, Writing – review & editing, Supervision. **Frédéric Vogel:** Methodology, Writing – review & editing, Funding acquisition, Supervision.

Declaration of Competing Interest

The authors declare that they have no known competing financial interests or personal relationships that could have appeared to influence the work reported in this paper.

Data availability

Data will be made available on request.

Acknowledgements

This project was financially supported by the Swiss National Science Foundation grants 200021_172624/1 and 200021_184817, as well as by the Swiss Innovation Agency Innosuisse and is part of the Swiss Competence Centre for Energy Research SCCER BIOSWEET. The authors would like to thank Erich De Boni and Pascal Unverricht for designing, optimising and keeping the continuous SCWG test rig running smoothly. We also thank Andrea Testino for helping with TGA measurements and Ivo Alxneit for some HR-TEM images. The Swiss National Science Foundation (R'Equip Project 206021_177020) is kindly acknowledged for the co-funding of the electron microscope.

Appendix A. Supporting information

Supplementary data associated with this article can be found in the online version at [doi:10.1016/j.apcatb.2022.121956](https://doi.org/10.1016/j.apcatb.2022.121956).

REFERENCES

- [1] M. Gassner, F. Vogel, G. Heyen, F. Maréchal, *Energy Environ. Sci.* 4 (2011) 1726–1741.
- [2] M. Modell, *Fundamentals of Thermochemical Biomass Conversion*, Springer, Dordrecht, 1985, pp. 95–119 (pp).
- [3] M.J. Antal, S.G. Allen, D. Schulman, X. Xu, R.J. Divilio, *Ind. Eng. Chem. Res.* 39 (2000) 4040–4053.
- [4] Y. Matsumura, T. Minowa, B. Potic, S.R.A. Kersten, W. Prins, W.P.M. van Swaaij, B. van de Beld, D.C. Elliott, G.G. Neuenschwander, A. Kruse, M. Jerry Antal Jr., *Biomass-- Bioenergy* 29 (2005) 269–292.
- [5] A. Kruse, *Biofuels, Bioprod. Bioref.* 2 (2008) 415–437.
- [6] D.C. Elliott, *Biofuels, Bioprod. Bioref.* 2 (2008) 254–265.
- [7] F. Vogel, *Synthetic Natural Gas from Coal, Dry Biomass, and Power-to-Gas Applications*, John Wiley & Sons, Inc., 2016, pp. 249–278 (pp).
- [8] F. Vogel, *Handbook of Green Chemistry*, John Wiley & Sons, Inc., 2010, pp. 281–324 (pp).
- [9] G. Peng, F. Vogel, D. Refardt, C. Ludwig, *Ind. Eng. Chem. Res.* 56 (2017) 6256–6265.
- [10] C. Hunston, D. Baudouin, M. Tarik, O. Kröcher, F. Vogel, *Catal. Sci. Technol.* 11 (2021), 7431–7344.
- [11] J.N. Jocz, L.T. Thompson, P.E. Savage, *Chem. Mater.* 30 (2018) 1218–1229.
- [12] S. Li, P.E. Savage, L. Guo, *J. Supercrit. Fluids* 135 (2018) 188–197.
- [13] Y. Wang, Y. Zhu, Z. Liu, L. Wang, D. Xu, C. Fang, S. Wang, *Int. J. Hydrol. Energy* 44 (2019) 3470–3480.
- [14] D.C. Elliott, M.R. Phelps, L.J. Sealock, E.G. Baker, *Ind. Eng. Chem. Res.* 33 (1994) 566–574.
- [15] G. Peng, C. Ludwig, F. Vogel, *Appl. Catal. B: Environ.* 202 (2017) 262–268.
- [16] M.H. Waldner, F. Krumeich, F. Vogel, *J. Supercrit. Fluids* 43 (2007) 91–105.
- [17] M. Dreher, B. Johnson, A.A. Peterson, M. Nachtegaal, J. Wambach, F. Vogel, *J. Catal.* 301 (2013) 38–45.
- [18] M. Osada, N. Hiyoshi, O. Sato, K. Arai, M. Shirai, *Energy Fuels* 21 (2007) 1400–1405.
- [19] D.J.M. de Vlieger, D.B. Thakur, L. Lefferts, K. Seshan, *ChemCatChem* 4 (2012) 2068–2074.
- [20] S. Bjelić, U. Gasser, I. Alxneit, F. Vogel, *ChemCatChem* 11 (2019) 1747–1755.
- [21] I. Behnia, Z. Yuan, P. Charpentier, C.C. Xu, *Fuel Process. Technol.* 143 (2016) 27–34.
- [22] P. Azadi, R. Farnood, *Int. J. Hydrol. Energy* 36 (2011) 9529–9541.
- [23] J.M.G. Carballo, J. Yang, A. Holmen, S. García-Rodríguez, S. Rojas, M. Ojeda, J.L. G. Fierro, *J. Catal.* 284 (2011) 102–108.
- [24] C.-x. Xiao, Z.-p. Cai, T. Wang, Y. Kou, N. Yan, *Angew. Chem. Int. Ed.* 47 (2008) 746–749.
- [25] C.J.H. Jacobsen, S. Dahl, P.L. Hansen, E. Törnqvist, L. Jensen, H. Topsøe, D.V. Prip, P.B. Mønshaug, I. Chorkendorff, *J. Mol. Catal. A: Chem.* 163 (2000) 19–26.
- [26] S. Dahl, A. Logadottir, R.C. Egeberg, J.H. Larsen, I. Chorkendorff, E. Törnqvist, J. K. Nørskov, *Phys. Rev. Lett.* 83 (1999) 1814–1817.
- [27] F.R. García-García, A. Guerrero-Ruiz, I. Rodríguez-Ramos, *Top. Catal.* 52 (2009) 758–764.
- [28] W. Raróg-Pilecka, D. Szmigiel, A. Komornicki, J. Zieliński, Z. Kowalczyk, *Carbon* 41 (2003) 589–591.
- [29] P. Panagiotopoulou, D.I. Kondarides, X.E. Verykios, *Appl. Catal. B: Environ.* 88 (2009) 470–478.
- [30] T. Abe, M. Tanizawa, K. Watanabe, A. Taguchi, *Energy Environ. Sci.* 2 (2009) 315–321.
- [31] E. Truszkiewicz, K. Zegadio, D. Wojda, B. Mierzwa, L. Kępiński, *Top. Catal.* 60 (2017) 1299–1305.
- [32] S.B. Vendelbo, M. Johansson, J.H. Nielsen, I. Chorkendorff, *Phys. Chem. Chem. Phys.* 13 (2011) 4486–4493.
- [33] R. van Hardeveld, A. van Montfoort, *Surf. Sci.* 4 (1966) 396–430.
- [34] M.P. Andersson, F. Abild-Pedersen, I.N. Remediakis, T. Bligaard, G. Jones, J. Engbæk, O. Lytken, S. Horch, J.H. Nielsen, J. Sehested, J.R. Rostrup-Nielsen, J. K. Nørskov, I. Chorkendorff, *J. Catal.* 255 (2008) 6–19.
- [35] L. Foppa, M. Iannuzzi, C. Copéret, A. Comas-Vives, *J. Catal.* 371 (2019) 270–275.
- [36] S. Shetty, A.P.J. Jansen, R.A. van Santen, *J. Phys. Chem. C* 112 (2008) 14027–14033.
- [37] I. Czekaj, S. Pin, J. Wambach, *J. Phys. Chem. C* 117 (2013) 26588–26597.
- [38] M. Osada, O. Sato, K. Arai, M. Shirai, *Energy Fuels* 20 (2006) 2337–2343.
- [39] M. Bagnoud-Velásquez, M. Brandenberger, F. Vogel, C. Ludwig, *Catal. Today* 223 (2014) 35–43.
- [40] D.J.M. de Vlieger, L. Lefferts, K. Seshan, *Green. Chem.* 16 (2014) 864–874.
- [41] G.L. Bezemer, J.H. Bitter, H.P.C.E. Kuipers, H. Oosterbeek, J.E. Holewijn, X. Xu, F. Kapteijn, A.J. van Dillen, K.P. de Jong, *J. Am. Chem. Soc.* 128 (2006) 3956–3964.
- [42] W.S. Lamme, J. Zečević, K.P. de Jong, *ChemCatChem* 10 (2018) 1552–1555.
- [43] B. He, Y. Zhang, X. Liu, L. Chen, *ChemCatChem* 12 (2020) 1853–1872.
- [44] G. Peng, C. Ludwig, F. Vogel, *ChemCatChem* 8 (2016) 139–141.
- [45] Y.-Q. Shan, L.-X. Yin, O.S. Djandja, Z.-C. Wang, P.-G. Duan, *Fuel* 292 (2021), 120288.
- [46] P.B. Weisz, C.D. Prater, *Adv. Catal.* 6 (1954) 143–196.
- [47] I. Alxneit, *J. Phys. Chem. A* 124 (2020) 10075–10081.
- [48] R. ColomaRibera, R.W.E. van de Kruijjs, S. Kokke, E. Zoethout, A.E. Yakshin, F. Bijkerk, *Appl. Phys. Lett.* 105 (2014), 131601.
- [49] D. Baudouin, U. Rodemerck, F. Krumeich, A. d. Mallmann, K.C. Szeto, H. Ménard, L. Veyre, J.-P. Candy, P.B. Webb, C. Thieuleux, C. Copéret, *J. Catal.* 297 (2013) 27–34.
- [50] K. Furman, D. Baudouin, T. Margossian, K.D. Sabnis, Y. Cui, F.H. Ribeiro, C. Copéret, *J. Catal.* 324 (2015) 9–13.
- [51] R. Van Hardeveld, F. Hartog, *Surf. Sci.* 15 (1969) 189–230.
- [52] M. Wolters, L.J.W. van Grotel, T.M. Eggenhuisen, J.R.A. Sietsma, K.P. de Jong, P. E. de Jongh, *Catal. Today* 163 (2011) 27–32.
- [53] J.R.A. Sietsma, J.D. Meeldijk, M. Versluijs-Helder, A. Broersma, A.J. v. Dillen, P. E. de Jongh, K.P. de Jong, *Chem. Mater.* 20 (2008) 2921–2931.
- [54] F. Winter, G. LeendertBezemer, C. van der Spek, J.D. Meeldijk, A. Jos, van Dillen, J. W. Geus, K.P. de Jong, *Carbon* 43 (2005) 327–332.
- [55] T.W. van Deelen, H. Yoshida, R. Oord, J. Zečević, B.M. Weckhuysen, K.P. de Jong, *Appl. Catal. A: Gen.* 593 (2020), 117441.
- [56] N.A. Krans, N. Ahmad, D. Alloyeau, K.P. de Jong, J. Zečević, *Micron* 117 (2019) 40–46.

- [57] S.C. Parker, C.T. Campbell, Phys. Rev. B 75 (2007), 035430.
- [58] P. Yin, S. Hu, K. Qian, Z. Wei, L.-L. Zhang, Y. Lin, W. Huang, H. Xiong, W.-X. Li, H.-W. Liang, Nat. Commun. 12 (2021) 4865.
- [59] G. Peng PhD thesis, EPFL, 2015.